

Density functional theory of fluids in nanopores: Analysis of the fundamental measures theory in extreme dimensional-crossover situations

A. González,^{a)} J. A. White,^{b)} F. L. Román,^{c)} and S. Velasco

Departamento de Física Aplicada, Universidad de Salamanca, E-37008 Salamanca, Spain

(Received 28 April 2006; accepted 21 June 2006; published online 8 August 2006)

Two density functional theories, the fundamental measures theory of Rosenfeld [Phys. Rev. Lett. **63**, 980 (1989)] and a subsequent approximation by Tarazona [Phys. Rev. Lett. **84**, 694 (2000)] are applied to the study of the hard-sphere fluid in two situations: the cylindrical pore and the spherical cavity. The results are compared with those obtained with grand canonical ensemble Monte Carlo simulations. The differences between both theories are evaluated and interpreted in the terms of the dimensional crossover from three to one and zero dimensions. © 2006 American Institute of Physics. [DOI: 10.1063/1.2227389]

I. INTRODUCTION

In 1989 Rosenfeld¹⁻³ developed a density functional theory for an inhomogeneous mixture of hard spheres. In this theory, the excess (over ideal) contribution $\mathcal{F}_{\text{ex}}[\rho]$ to the free-energy functional is assumed to take the form

$$\beta\mathcal{F}_{\text{ex}}[\rho] = \beta\mathcal{F}[\rho] - \beta\mathcal{F}_{\text{id}}[\rho] = \int d\mathbf{r}\Phi[\rho], \quad (1)$$

where, for the sake of simplicity, we have restricted ourselves to the one-component fluid with density $\rho(\mathbf{r})$. In this equation $\beta^{-1}\Phi$ is the excess free-energy density and it can be expressed as a function of two scalar weighted densities, $\eta(\mathbf{r})$ and $n(\mathbf{r})$, and one vector weighted density, $\mathbf{v}(\mathbf{r})$, which are defined by

$$\eta(\mathbf{r}) = \int_{|\mathbf{r}-\mathbf{r}'|<R} \rho(\mathbf{r}')d\mathbf{r}' = \int \rho(\mathbf{r}')\theta(R-|\mathbf{r}-\mathbf{r}'|)d\mathbf{r}', \quad (2)$$

$$n(\mathbf{r}) = \frac{1}{4\pi R^2} \int \rho(\mathbf{r}')\delta(R-|\mathbf{r}-\mathbf{r}'|)d\mathbf{r}', \quad (3)$$

$$\mathbf{v}(\mathbf{r}) = \frac{1}{4\pi R^2} \int \rho(\mathbf{r}')\delta(R-|\mathbf{r}-\mathbf{r}'|)(\widehat{\mathbf{r}-\mathbf{r}'}d\mathbf{r}', \quad (4)$$

where $R=\sigma/2$ is the radius of the hard spheres and $\hat{\mathbf{r}}\equiv\mathbf{r}/r$ is a unit vector. The weight functions used in Eqs. (2)–(4) are related to the fundamental geometric measures of the sphere, and consequently this theory and more recent versions⁴⁻²⁶ based on these measures are called fundamental measures theories (FMTs). In the present work we shall denote the original Rosenfeld's version¹⁻³ of the FMT as OFMT. The

excess free-energy density for the OFMT can be written as a sum of three contributions,

$$\Phi_{\text{OFMT}} = \Phi_1 + \Phi_2 + \Phi_3, \quad (5)$$

where

$$\Phi_1 = -n(\mathbf{r})\log[1 - \eta(\mathbf{r})], \quad (6)$$

$$\Phi_2 = 4\pi R^3 \frac{n(\mathbf{r})^2 - \mathbf{v}(\mathbf{r}) \cdot \mathbf{v}(\mathbf{r})}{1 - \eta(\mathbf{r})}, \quad (7)$$

$$\Phi_3 = 8\pi^2 R^6 n(\mathbf{r}) \frac{\frac{1}{3}n(\mathbf{r})^2 - \mathbf{v}(\mathbf{r}) \cdot \mathbf{v}(\mathbf{r})}{[1 - \eta(\mathbf{r})]^2}. \quad (8)$$

In its different versions, the FMT has been applied to a large number of inhomogeneous situations with excellent agreement with simulation results. Kierlik and co-workers have applied their own version of the FMT to adsorption at planar walls.⁴⁻⁶ This problem was also addressed by Roth and Dietrich²⁷ using the OFMT and later on by Roth *et al.*²⁵ using the so-called White Bear version of the FMT^{25,26} which is based on the accurate Boublik, Mansoori *et al.* equation of state.^{28,29} González *et al.* have compared simulation data with FMT results for the hard-sphere fluid at a hard wall,^{14,15} inside a spherical cavity³⁰⁻³³ and for the two-body¹⁴ and three-body³⁴ correlation functions. Cuesta¹¹ and Cuesta and Martínez-Ratón^{12,13} have developed a FMT formalism for mixtures of parallel hard cubes. Lafuente and Cuesta²⁴ considered the FMT description of lattice fluids and Schmidt formulated FMT versions for penetrable spheres,¹⁶ colloid-polymer mixtures,¹⁷ and soft interactions.¹⁸⁻²⁰ Other successful applications of the FMT include studies of adsorption near structured and curved substrates³⁵⁻³⁷ as well as in cylindrical pores³⁸ and in rectangular microchannels.³⁹

The main drawback of the OFMT relies on the fact that it cannot account properly for the solid-fluid transition as well as for extreme quasi-zero-dimensional (quasi-0D) situations. The reason for this failure is the appearance of non-integrable divergences in the strict 0D limit of the theory.^{8,9}

^{a)} Author to whom correspondence should be addressed. Electronic mail: ags@usal.es

^{b)} Electronic mail: white@usal.es

^{c)} Also at Departamento de Física Aplicada, Escuela Politécnica Superior de Zamora, Universidad de Salamanca, E-49022 Zamora, Spain.

The importance of this limit can be clearly understood by considering that in the solid, at close packing, a particle is surrounded by its neighbors so closely that a quasi-0D situation arises. Consequently, any theory willing to describe appropriately the solid-fluid transition should also properly describe situations where the dimensionality of the system is reduced to two dimensions (2D), one dimension (1D), and even 0D, i.e., the theory must exhibit the right *dimensional crossover*.

More recent versions of the FMT have been developed with the requirement of having the correct dimensional crossover.⁸⁻¹⁰ In this context, a new functional was recently proposed by Tarazona^{21,22} by considering a *dimensional interpolation* scheme between the exact result for a wide class of zero-dimensional cavities and the three-dimensional hard-sphere fluid. This cavity fundamental measures theory (CFMT) is based on the following expression for the excess free-energy density:²²

$$\Phi_{\text{CFMT}} = \Phi_1 + \Phi_2 + \bar{\Phi}_3, \quad (9)$$

where the Φ_1 and Φ_2 terms coincide with the corresponding ones of the OFMT and the new term $\bar{\Phi}_3$ can be written as

$$\bar{\Phi}_3 = 12\pi^2 R^6 \frac{f_3(\mathbf{r})}{[1 - \eta(\mathbf{r})]^2}, \quad (10)$$

with

$$f_3(\mathbf{r}) = \mathbf{v} \cdot \mathbf{T} \cdot \mathbf{v} - n\mathbf{v} \cdot \mathbf{v} - \text{Tr}[\mathbf{T}^3] + n \text{Tr}[\mathbf{T}^2], \quad (11)$$

where $\text{Tr}[\dots]$ denotes the trace operator and \mathbf{T} is a tensor weighted density with Cartesian components

$$\mathbf{T}_{\alpha,\beta} = \frac{1}{4\pi R^2} \int \rho(\mathbf{r}') \delta(R - |\mathbf{r} - \mathbf{r}'|) (\widehat{\mathbf{r} - \mathbf{r}'})_\alpha (\widehat{\mathbf{r} - \mathbf{r}'})_\beta d\mathbf{r}', \quad (12)$$

where α and β run over x, y and z and $(\widehat{\mathbf{r} - \mathbf{r}'})_\alpha$ denotes the corresponding component of the unit vector $(\widehat{\mathbf{r} - \mathbf{r}'})$. By construction this theory gives rise to the exact 1D free energy (something already met with $\Phi_1 + \Phi_2$ alone) and to the exact 0D limit (except for a few 0D *lost cases*¹⁰). Furthermore, the CFMT has been shown to accurately describe the freezing of hard spheres.²¹ Finally, we would like to note that the CFMT can be formulated to reproduce the accurate Carnahan-Starling equation of state⁴⁰ by a simple modification of the dependence with $\eta(\mathbf{r})$ of $\bar{\Phi}_3$ in Eq. (10) (see Ref. 22).

It becomes clear that the CFMT should perform at its best for fluids in which the geometry and the confinement constraints lead to quasi-1D or quasi-0D situations where the OFMT might fail. Therefore, it seems interesting to look for possible scenarios where this kind of situations could come into play. In this work we shall compare the performance of both FMT theories for a hard-sphere fluid confined to a hard cylindrical pore of radius R_c and to a hard spherical cavity of radius R_s that, respectively, can give rise to quasi-1D and quasi-0D confinements.

This work is organized as follows. In Sec. II we present the main steps for obtaining the equilibrium density profile.

In Sec. III the results of both theories are compared with simulation data. We conclude with a brief summary of the paper.

II. THE EQUILIBRIUM DENSITY PROFILE

The equilibrium density profile $\rho(\mathbf{r})$ of a fluid in the grand canonical ensemble with chemical potential μ and subjected to an external potential $V_{\text{ext}}(\mathbf{r})$ is the solution of the well known Euler-Lagrange equation

$$\frac{\delta \mathcal{F}[\rho]}{\delta \rho(\mathbf{r})} + V_{\text{ext}}(\mathbf{r}) = \mu, \quad (13)$$

which can be rewritten as³¹

$$\Lambda^3 \rho(\mathbf{r}) = \exp[c^{(1)}(\mathbf{r}) + \beta\mu - \beta V_{\text{ext}}(\mathbf{r})], \quad (14)$$

where Λ is the thermal de Broglie wavelength and $c^{(1)}(\mathbf{r})$ is the one-body direct correlation function:⁴¹

$$c^{(1)}(\mathbf{r}) = -\beta \frac{\delta \mathcal{F}_{\text{ex}}[\rho]}{\delta \rho(\mathbf{r})}. \quad (15)$$

The equilibrium density profile is obtained by solving Eq. (14) by means of an iterative process which requires the evaluation of $c^{(1)}(\mathbf{r})$. In order to obtain an explicit expression for $c^{(1)}(\mathbf{r})$, it is convenient to rewrite the excess free-energy contribution (1) in the following form:

$$\beta \mathcal{F}_{\text{ex}}[\rho] = \int d\mathbf{r} \Phi(\{m_i(\mathbf{r})\}), \quad (16)$$

where $\{m_i(\mathbf{r})\}$ is a set of scalar quantities, namely,

$$\{m_i(\mathbf{r})\} = \{\eta, n, \mathbf{v} \cdot \mathbf{v}, \mathbf{v} \cdot \mathbf{T} \cdot \mathbf{v}, \text{Tr}[\mathbf{T}^2], \text{Tr}[\mathbf{T}^3]\}. \quad (17)$$

From Eq. (16) one obtains

$$c^{(1)}(\mathbf{r}) = - \int d\mathbf{r}' \sum_i \Phi_{m_i}(\mathbf{r}') \frac{\delta m_i(\mathbf{r}')}{\delta \rho(\mathbf{r})}, \quad (18)$$

where $\Phi_{m_i} \equiv \partial \Phi / \partial m_i$. Therefore, the calculation of the equilibrium density profile requires the following steps: (i) calculation of the $m_i(\mathbf{r})$'s, (ii) evaluation of the functional derivatives $\delta m_i(\mathbf{r}') / \delta \rho(\mathbf{r})$, and (iii) calculation of $c^{(1)}(\mathbf{r})$ via Eq. (18). The three steps are notably simplified by taking into account the symmetry of the external potential $V_{\text{ext}}(\mathbf{r})$. As we show in Appendix A, all calculations can be reduced to convolutions that can be conveniently handled by means of the Fourier techniques sketched in Appendix B.

In order to test the performance of the two density functional theories considered in this work, we have also made grand canonical ensemble Monte Carlo (GCEMC) simulations⁴² of a hard-sphere fluid in a cylindrical pore⁴³ and a spherical cavity.³¹ The simulation consists of a series of Monte Carlo steps (MCSs) in which attempts to change the system configuration via particle displacement or particle insertion or removal are selected with equal probability. In the first case a particle is chosen at random and is given a random displacement which is rejected in case of overlap with another particle or with the pore walls. In the second

case one performs with equal probability an insertion or a removal attempt. A removal attempt is accepted with probability

$$\text{acc}(N \rightarrow N-1) = \min\left[1, \frac{N}{zV}\right], \quad (19)$$

where $z \equiv \Lambda^{-3} e^{\beta\mu}$ and V is the volume in the pore accessible to the center of a particle. An insertion attempt is accepted with probability

$$\text{acc}(N \rightarrow N+1) = \min\left[1, \frac{zV}{N+1}\right]. \quad (20)$$

In this case the new particle is located at a random position inside the pore. In case of overlap the insertion attempt is rejected.

In the case of the cylindrical pore, we have considered 10^7 MCSs to equilibrate the system followed by 10^8 MCSs where the profile is measured every $\langle N \rangle$ MCSs. For this particular geometry, periodic boundary conditions along the Z axis have been employed, being the length of the cylindrical pore equal to 10σ . In the spherical cavity the simulations consist in 10^9 equilibration MCSs followed by 2×10^9 MCSs to perform the measurements (every $\langle N \rangle$ steps).

The probability of particle insertion or removal is determined in the GCEMC simulation by the parameter z together with the geometry of the pore, and therefore, for a given pore, z determines the state of the system. Since we are working in the grand canonical ensemble, the value of z (or, equivalently, μ) is the same for the bulk fluid that acts as a particle reservoir. In this context, we note that the (bulk) density of the reservoir ρ_B is related to μ and z via Eq. (14) which for a homogeneous fluid becomes

$$\Lambda^3 \rho_B = \exp[c^{(1)}(\rho_B) + \beta\mu], \quad (21)$$

and thus

$$z = \rho_B \exp[-c^{(1)}(\rho_B)]. \quad (22)$$

An accurate expression for the one-body direct correlation function of the bulk fluid $c^{(1)}(\rho_B)$ can be obtained from the Carnahan-Starling (CS) equation of state. One has

$$-c_{\text{CS}}^{(1)}(\rho_B) = \eta \frac{8 - 9\eta + 3\eta^2}{(1 - \eta)^3}, \quad (23)$$

where $\eta \equiv \pi\rho_B/6$ is the packing fraction of the reservoir.

Using Eqs. (22) and (23) one can specify the state of the system by fixing the value of ρ_B and this is the method that we have followed in our simulations. In principle one could follow the same method for the FMT calculations. However, the FMT prescriptions considered in the present work give rise to the Percus-Yevick (PY) free energy for the homogeneous fluid and thus to a different value of μ and z . In order to avoid this problem and since we are interested in comparing the results of the FMT calculations with simulation data, we have chosen to solve the Euler-Lagrange equation for the density profile in the spherical cavity in such a way that it yields the same mean number of particles $\langle N \rangle$ than the simulation result (see Ref. 31 for details). Of course, in the case of the cylindrical pore, one has to fix the value of $\langle N \rangle/L$.

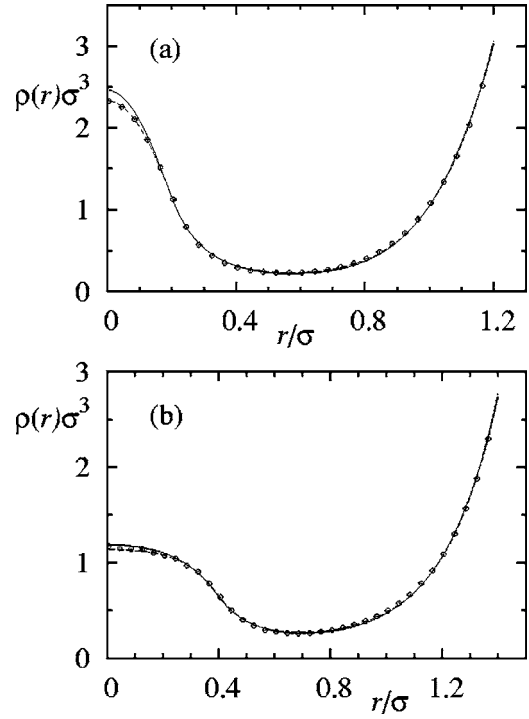


FIG. 1. Density profiles of hard spheres in a cylindrical pore, $\rho_B = 0.55\sigma^{-3}$. (a) $R_c = 1.7\sigma$ and (b) $R_c = 1.9\sigma$. The symbols are the results of the GCEMC simulations. The solid and dashed lines are the results of the OFMT and the CFMT, respectively.

III. RESULTS

In this section we compare the results of the two versions of the FMT with simulation data. We start with the cylindrical pore and then we consider a spherical cavity. Since the most relevant differences between the results of both theories arise in quasi-1D or quasi-0D situations, we consider pores with very small radii ($R_{c,s} \sim 1.2\sigma - 2.5\sigma$).

A. Cylindrical pore

Figure 1 shows the results of theory and simulation for the density profile of a hard-sphere fluid in a cylindrical pore at intermediate packing. In general the two FMT prescriptions and the GCEMC simulation give very similar results. One can observe, however, that small differences do arise between the OFMT and the CFMT results in the center of the cylinder. These differences are larger in Fig. 1(a) where the peak is more pronounced. As expected, the CFMT yields better results for this central zone than the OFMT. This behavior is a signature of the correct dimensional-crossover properties of the CFMT that begin to manifest at moderate packings.

At higher packings we obtain profiles like the ones presented in Fig. 2. When compared with Fig. 1 one can observe that the situation is now much more inhomogeneous (note the vertical scales). In spite of this, both FMTs continue to give good results, although there are regions where differences with simulation appear. It is interesting to verify that both theories have difficulties to follow the birth of the central peak [see Fig. 2(a)]. However, in Fig. 2(b), when this peak is fully developed, the CFMT still gives an accurate

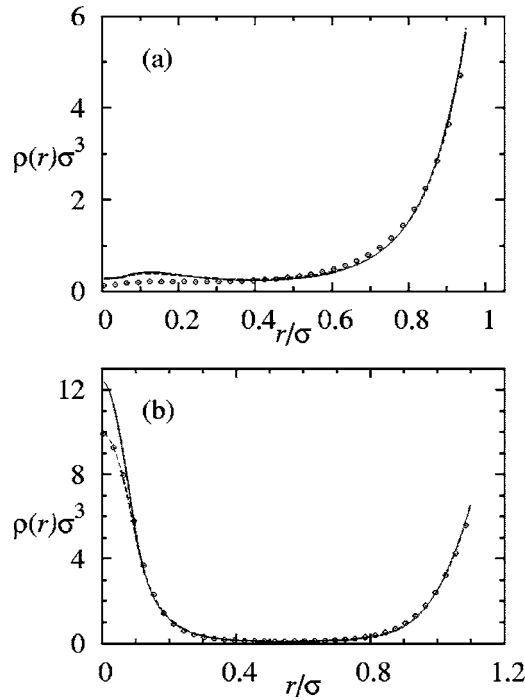


FIG. 2. Density profiles of hard spheres in a cylindrical pore, $\rho_B = 0.7\sigma^{-3}$. (a) $R_c = 1.45\sigma$ and (b) $R_c = 1.60\sigma$. The symbols are the results of the GCEMC simulations. The solid and dashed lines are the results of the OFMT and the CFMT, respectively.

description of the profile while the OFMT overestimates the peak at the center of the cylinder. The peak indicates a zone of strong localization in the center of the pore which is related to a quasi-1D situation accurately described by the CFMT.

By varying the radius of the cylinder, it is possible to find situations where the density profile at the center exhibits a minimum rather than a maximum. In these situations both FMT prescriptions should yield very similar results (one must keep in mind that the main difference between the OFMT and the CFMT concerns the one- and zero-dimensional limits). Figure 3 shows two examples of this behavior. As expected, the differences between OFMT and CFMT are negligible. Note that both FMT results are very accurate with only minor discrepancies at contact and in the regions of $r \approx 0.55\sigma$ [Fig. 3(a)] and $r \approx 0.9\sigma$ [Fig. 3(b)].

In the preceding figures, we have seen that at constant ρ_B , the density profile at the center of the pore can vary from a pronounced peak to a well defined valley, indicating an oscillating behavior that depends on the radius of the cylindrical pore R_c . This behavior is clearly related to the creation of new layers in the fluid from a mechanism based on the birth and death of quasi-1D situations at different radii. Figure 4 shows the results of theory and simulation for the density at the center of the pore as a function of the radius R_c for two different values of ρ_B . For clarity we only plot results for R_c ranging between 1.3σ and 2.5σ (about one oscillation period). As suggested by Ref. 33, the value of the density at the center of the pore has been estimated in simulation by measuring the mean density $\hat{\rho}$ in a small cylinder of radius $r_c = 0.05\sigma$ situated at the center of the pore. For consistency, the FMT results have been obtained using $\hat{\rho}$

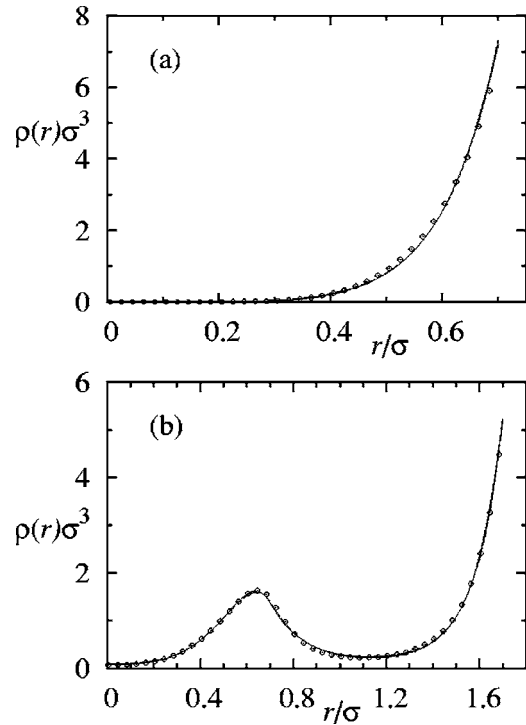


FIG. 3. Density profiles of hard spheres in a cylindrical pore, $\rho_B = 0.7\sigma^{-3}$. (a) $R_c = 1.2\sigma$ and (b) $R_c = 2.2\sigma$. The symbols are the results of the GCEMC simulations. The solid and dashed lines are the results of the OFMT and the CFMT, respectively.

$= \int_0^{r_c} \rho(r) 2\pi r dr / (\pi r_c^2)$. From Fig. 4 it is clear that while the CFMT is able to accurately account for the evolution of the density at the center of the cylinder, the OFMT results show appreciable differences with simulation, especially when the peak is fully developed or starting to vanish. As expected, the behavior of the OFMT becomes worse at higher packings [Fig. 4(b)].

B. Spherical cavity

Figure 5 shows the results of theory and simulation for the density profile of a hard-sphere fluid in a spherical cavity at intermediate packing. Comparing with the results for the cylindrical pore, we obtain a very similar behavior in general. However, we note that, for a given value of the density of the particle reservoir ρ_B , the packing constraints in the spherical cavity lead the system to a situation more inhomogeneous than in the cylindrical pore. This can be seen, for instance, by comparing Fig. 1(a) with Fig. 5(a). This is related to the fact that the geometry of the spherical confinement gives rise to quasi-0D situations in the center of the cavity, in contrast to the quasi-1D situations that arise in the cylindrical pore. Therefore, it is no surprising that the FMT results are slightly worse (although still very good) for this geometry. Again, when a central peak is fully developed [Fig. 5(a)], the CFMT results are accurate while the OFMT results show important discrepancies with the GCEMC simulation data. In this case, the observed discrepancies are due to the failure of the OFMT to account for a quasi-zero-dimensional situation.

At higher packings, the OFMT results become worse, and, eventually, we arrive to situations like that of Fig. 6

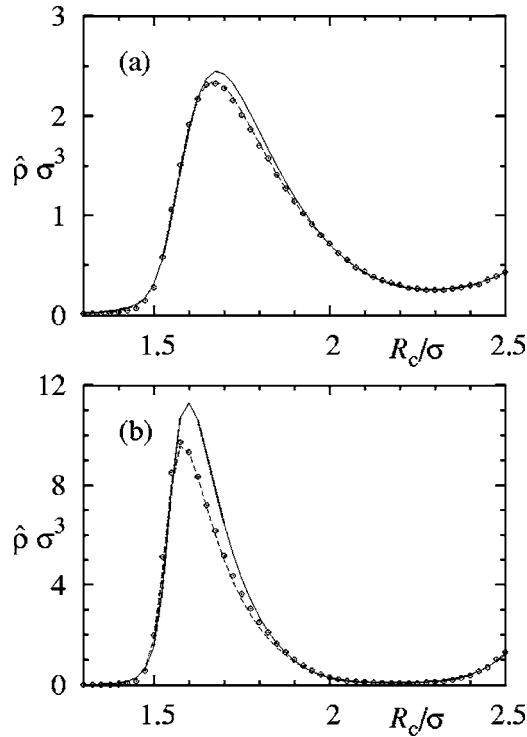


FIG. 4. Mean density at the center of a cylindrical pore. (a) $\rho_B=0.55\sigma^{-3}$ and (b) $\rho_B=0.7\sigma^{-3}$. The symbols are the results of the GCEMC simulations. The solid and dashed lines are the results of the OFMT and the CFMT, respectively.

where we are unable to find a numerical solution of the Euler-Lagrange equation for the system (see also Fig. 8). It is remarkable, however, that the CFMT is still able to give accurate results for this extremely inhomogeneous quasi-0D situation.

Like in the case of the cylindrical pore, it is possible to find situations where the density profile exhibits a minimum in the center of the cavity (see Fig. 7). In these situations, both theories yield very similar results which in general are very accurate.

The behavior of the density at the center of the cavity as a function the radius of the spherical cavity R_s is shown in Fig. 8 for two different values of ρ_B . Like in the cylindrical pore, the value of the density has been estimated in simulation by measuring the mean density $\hat{\rho}$ in a small sphere of radius $r_s=0.05\sigma$ located at the center of the cavity. The results of the FMT for $\hat{\rho}$ can be easily obtained from $\hat{\rho} = \int_0^{r_s} \rho(r) 4\pi r^2 dr / (\frac{4}{3}\pi r_s^3)$. Like in the preceding cylindrical geometry, the CFMT yield results in excellent agreement with simulation data while the OFMT fails when the density in the center reaches its maximum and for larger values of R_c when its value begins to decrease. This behavior is stressed when the value of ρ_B increases. We note that for this geometry the peak in the center of the cavity is related to a quasi-0D situation and thus the OFMT yields less accurate results than in the cylindrical cavity where a quasi-1D can take place.

IV. SUMMARY

We have applied two versions of the FMT—the original prescription due to Rosenfeld and a subsequent modification

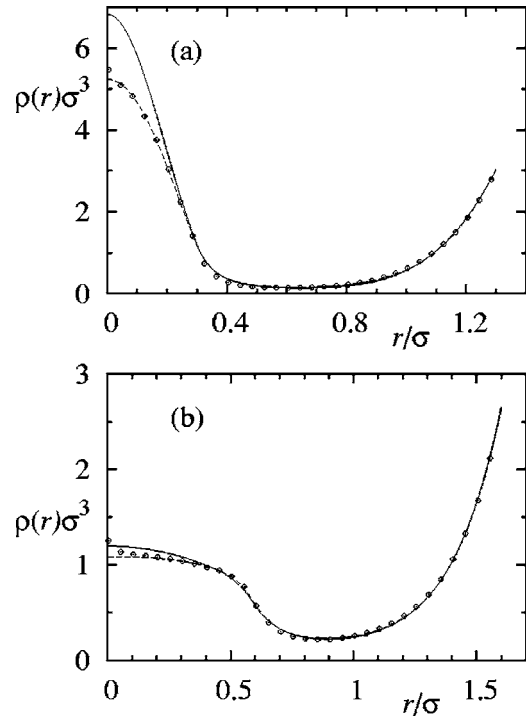


FIG. 5. Density profiles of hard spheres in a spherical cavity, $\rho_B=0.5\sigma^{-3}$. (a) $R_s=1.8\sigma$ and (b) $R_s=2.1\sigma$. The symbols are the results of the GCEMC simulations. The solid and dashed lines are the results of the OFMT and the CFMT, respectively.

by Tarazona—to the study of a hard-sphere fluid subjected to two different confinement potentials: a cylindrical pore and a spherical cavity. The interest of these geometries is that, under certain conditions, the fluid at the center of the cavities can give rise to quasi-1D and quasi-0D situations, respectively.

This effective dimensional reduction is a severe test for the two FMTs considered in this work. In general, the results obtained from both theories are in good agreement with simulation. There are situations, however, where the results of Tarazona's CFMT are significantly better than those obtained with the OFMT, specially for the spherical (zero-dimensional) geometry. These differences can be ascribed to the poor behavior of the OFMT in quasi-1D and quasi-0D situations.

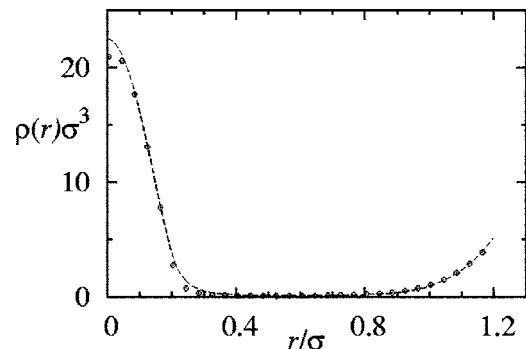


FIG. 6. Density profiles of hard spheres in a spherical cavity, $\rho_B=0.6\sigma^{-3}$ and $R_s=1.7\sigma$. The symbols are the results of the GCEMC simulations. The dashed lines are the results of the CFMT.

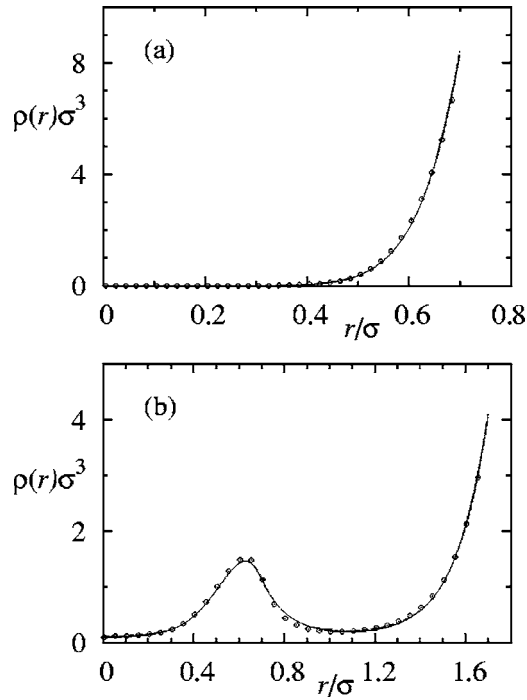


FIG. 7. Density profiles of hard spheres in a spherical cavity, $\rho_B = 0.6\sigma^{-3}$. (a) $R_s = 1.2\sigma$ and (b) $R_s = 2.2\sigma$. The symbols are the results of the GCEMC simulations. The solid and dashed lines are the results of the OFMT and the CFMT, respectively.

ACKNOWLEDGMENTS

We are grateful for financial support from the Ministerio de Ciencia y Tecnología of Spain under Grant Nos. BFM2003-07106 FEDER and FIS2005-05081 FEDER and from Junta de Castilla y León under Grant No. SA092/04.

APPENDIX A: STEPS IN THE CALCULATION OF THE EQUILIBRIUM PROFILE

In Sec. II we presented the main steps in the calculation of the equilibrium density profile from the two FMT prescriptions considered in this work. In this appendix we show how these steps can be reduced to convolutions that take profit of the symmetry of the problem.

1. Calculation of the $m_l(r)$'s

a. η and n

Equations (2) and (3) show that $\eta(\mathbf{r})$ and $n(\mathbf{r})$ are already expressed as the convolution of the density $\rho(\mathbf{r})$ times a weight function, i.e.,

$$\eta(\mathbf{r}) = \rho \otimes \omega_\eta, \quad (\text{A1})$$

$$\rho(\mathbf{r}) = \rho \otimes \omega_n, \quad (\text{A2})$$

where $\omega_\eta(r) = \theta(R-r)$ and $\omega_n(r) = \delta(R-r)/4\pi R^2$. These convolutions are appropriately handled in Fourier space by means of the convolution theorem. Taking into account that ω_η and ω_n only depend on the radial coordinate r , their Fourier transforms are given by

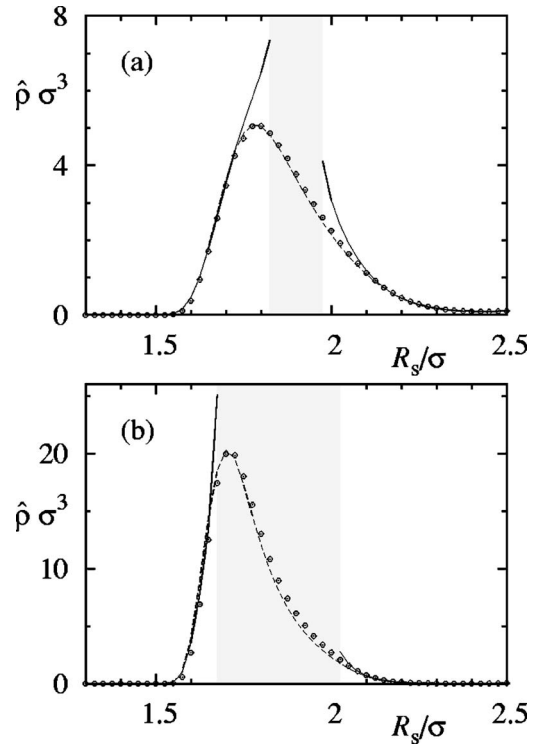


FIG. 8. Mean density at the center of a spherical cavity. (a) $\rho_B = 0.5\sigma^{-3}$ and (b) $\rho_B = 0.6\sigma^{-3}$. The symbols are the results of the GCEMC simulations. The solid and dashed lines are the results of the OFMT and the CFMT, respectively. The shaded areas represent the regions where, using the OFMT, we are unable to find a numerical solution for the density profile.

$$\tilde{\omega}_\eta(k) = \frac{4\pi}{k^3}(\sin kR - kR \cos kR), \quad (\text{A3})$$

$$\tilde{\omega}_n(k) = \frac{\sin kR}{kR}, \quad (\text{A4})$$

where $k = |\mathbf{k}|$.

For spherical symmetry $\rho = \rho(r)$ and therefore its Fourier transform is a function of k that can be obtained numerically from a 1D fast Fourier transform. Multiplying $\tilde{\rho}(k)$ by $\tilde{\omega}_\eta(k)$ [$\tilde{\omega}_n(k)$] and performing the inverse transform, one obtains $\eta(r)$ [$n(r)$].

In cylindrical symmetry the density profile only depends on the radial coordinate $\varrho = \sqrt{x^2 + y^2}$ and thus its Fourier transform becomes

$$\tilde{\rho}(\mathbf{k}) = 2\pi\delta(k_z) \int \rho(\varrho) \exp(i\mathbf{q} \cdot \boldsymbol{\varrho}) d\boldsymbol{\varrho}, \quad (\text{A5})$$

where $\boldsymbol{\varrho} = (x, y, 0)$ is a vector perpendicular to the axis of the cylinder and $\mathbf{q} = (k_x, k_y, 0)$. Thus $\tilde{\rho}(\mathbf{k})$ reduces to the product of a delta function times a 2D Fourier transform of the density. The latter can be further reduced so that one has

$$\tilde{\rho}(\mathbf{k}) = 2\pi\delta(k_z)\tilde{\rho}_H(q), \quad (\text{A6})$$

where $q = |\mathbf{q}|$ and $\tilde{\rho}_H$ is a 1D Hankel transform that can be evaluated numerically using the method presented in Appendix B. Taking into account Eq. (A6), one finally obtains that the convolution $\rho \otimes \omega$ is the inverse Hankel transform of the product $\tilde{\rho}_H(q)\omega(k)|_{k_z=0} = \tilde{\rho}_H(q)\omega(q)$.

b. $\mathbf{v} \cdot \mathbf{v}$

We first obtain the expression for $\mathbf{v} \cdot \mathbf{v}$ in cylindrical symmetry and then we quote the results for the simpler case of spherical symmetry.

It is not difficult to realize that in cylindrical symmetry, the vector weighted density \mathbf{v} introduced in (4) can be rewritten as

$$\mathbf{v}(\varrho) = \frac{1}{4\pi R^3} \int \rho(\varrho') \delta(R - |\mathbf{r} - \mathbf{r}'|) (\mathbf{r} - \mathbf{r}') d\mathbf{r}' = v(\varrho) \hat{\boldsymbol{\rho}}, \quad (\text{A7})$$

where v is a function that only depends on the radial coordinate ϱ and $\hat{\boldsymbol{\rho}} = \boldsymbol{\rho}/\varrho$. Multiplying Eq. (A7) by $\boldsymbol{\rho}$ and taking into account the identities

$$\boldsymbol{\rho} \cdot (\mathbf{r} - \mathbf{r}') = \frac{1}{2}(\varrho^2 - \varrho'^2 + (\mathbf{r} - \mathbf{r}')^2 - (z - z')^2) \quad (\text{A8})$$

and

$$\eta(\varrho) = \frac{1}{R} \int \rho(\varrho') (z - z')^2 \delta(R - |\mathbf{r} - \mathbf{r}'|) d\mathbf{r}', \quad (\text{A9})$$

we obtain

$$v(\varrho) = \frac{1}{2R\varrho} \left[(\varrho^2 + R^2)n(\varrho) - n_2(\varrho) - \frac{\eta(\varrho)}{4\pi R} \right], \quad (\text{A10})$$

where

$$n_2(\varrho) = \frac{1}{4\pi R^2} \int \varrho'^2 \rho(\varrho') \delta(R - |\mathbf{r} - \mathbf{r}'|) d\mathbf{r}' = (\varrho^2 \rho) \otimes \omega_n. \quad (\text{A11})$$

Finally, from (A7) one has

$$\mathbf{v} \cdot \mathbf{v} = v^2(\varrho). \quad (\text{A12})$$

In spherical symmetry $\rho = \rho(r)$, $\mathbf{v}(\mathbf{r}) = v(r)\hat{\mathbf{r}}$, and $\mathbf{v} \cdot \mathbf{v} = v^2(r)$. In this case we obtain

$$v(r) = \frac{1}{2Rr} [(r^2 + R^2)n(r) - n_2(r)], \quad (\text{A13})$$

where now $n_2(r) = (r^2 \rho) \otimes \omega_n$.

c. $\mathbf{v} \cdot \mathbf{T} \cdot \mathbf{v}$, $\text{Tr}[\mathbf{T}^2]$, and $\text{Tr}[\mathbf{T}^3]$

In cylindrical symmetry the tensor weighted density \mathbf{T} introduced in (12) becomes

$$\mathbf{T} = \begin{pmatrix} A(\varrho) + B(\varrho)x^2 & B(\varrho)xy & 0 \\ B(\varrho)yx & A(\varrho) + B(\varrho)y^2 & 0 \\ 0 & 0 & C(\varrho) \end{pmatrix}, \quad (\text{A14})$$

where A , B , and C are auxiliary functions that only depend on the radial coordinate ϱ . From definition (12) and Eq. (A9), one has

$$C(\varrho) = \frac{\eta(\varrho)}{4\pi R^3}, \quad (\text{A15})$$

and also, from (12), the trace of the tensor weighted density \mathbf{T} is given by

$$\text{Tr}[\mathbf{T}] = \rho \otimes \omega_n = 2A(\varrho) + B(\varrho)\varrho^2 + C(\varrho), \quad (\text{A16})$$

where we used Eq. (A14). A further relation between A and B can be obtained by noting that, on one hand, using Eq. (A14) we obtain

$$\boldsymbol{\rho} \cdot \mathbf{T} \cdot \boldsymbol{\rho} = A(\varrho)\varrho^2 + B(\varrho)\varrho^4, \quad (\text{A17})$$

and, on the other hand, from Eqs. (12) and (A8) one has

$$\boldsymbol{\rho} \cdot \mathbf{T} \cdot \boldsymbol{\rho} = \frac{1}{16\pi R^4} \int \rho(\varrho') \delta(R - |\mathbf{r} - \mathbf{r}'|) [\varrho^2 - \varrho'^2 + (\mathbf{r} - \mathbf{r}')^2 - (z - z')^2]^2 d\mathbf{r}', \quad (\text{A18})$$

which, as we did with the product $\mathbf{v} \cdot \mathbf{v}$, can be rewritten in terms of convolutions (not shown). From (A15)–(A18) one can obtain $A(\varrho)$, $B(\varrho)$, and $C(\varrho)$. Once these functions are known, one can evaluate $\mathbf{v} \cdot \mathbf{T} \cdot \mathbf{v}$, $\text{Tr}[\mathbf{T}^2]$, and $\text{Tr}[\mathbf{T}^3]$. From Eqs. (A7) and (A14), after some algebra, one obtains

$$\mathbf{v} \cdot \mathbf{T} \cdot \mathbf{v} = (A(\varrho) + B(\varrho)\varrho^2)v^2(\varrho), \quad (\text{A19})$$

$$\text{Tr}[\mathbf{T}^2] = (A(\varrho) + B(\varrho)\varrho^2)^2 + A^2(\varrho) + C^2(\varrho), \quad (\text{A20})$$

$$\text{Tr}[\mathbf{T}^3] = (A(\varrho) + B(\varrho)\varrho^2)^3 + A^3(\varrho) + C^3(\varrho). \quad (\text{A21})$$

In spherical symmetry the tensor weighted density \mathbf{T} becomes

$$\mathbf{T} = \begin{pmatrix} A(r) + B(r)x^2 & B(r)xy & B(r)xz \\ B(r)yx & A(r) + B(r)y^2 & B(r)yz \\ B(r)zx & B(r)zy & A(r) + B(r)z^2 \end{pmatrix}, \quad (\text{A22})$$

where now A and B are auxiliary functions that only depend on r and can be obtained proceeding like in cylindrical symmetry. From Eq. (A22) one obtains

$$\mathbf{v} \cdot \mathbf{T} \cdot \mathbf{v} = (A(r) + B(r)r^2)v^2(r), \quad (\text{A23})$$

$$\text{Tr}[\mathbf{T}^2] = (A(r) + B(r)r^2)^2 + 2A^2(r), \quad (\text{A24})$$

$$\text{Tr}[\mathbf{T}^3] = (A(r) + B(r)r^2)^3 + 2A^3(r). \quad (\text{A25})$$

2. Evaluation of the functional derivatives $\delta m_i(\mathbf{r}')/\delta \rho(\mathbf{r})$

From definitions (2) and (3) it is direct to obtain

$$\frac{\delta \eta(\mathbf{r}')}{\delta \rho(\mathbf{r})} = \omega_n(|\mathbf{r}' - \mathbf{r}|), \quad \frac{\delta n(\mathbf{r}')}{\delta \rho(\mathbf{r})} = \omega_n(|\mathbf{r}' - \mathbf{r}|), \quad (\text{A26})$$

while, from Eqs. (4) and (12), one has

$$\frac{\delta \mathbf{v}(\mathbf{r}')}{\delta \rho(\mathbf{r})} = \omega_n(|\mathbf{r}' - \mathbf{r}|)(\mathbf{r}' - \mathbf{r})/R, \quad (\text{A27})$$

$$\frac{\delta \mathbf{T}_{\alpha\beta}(\mathbf{r}')}{\delta \rho(\mathbf{r})} = \omega_n(|\mathbf{r}' - \mathbf{r}|)(\mathbf{r}' - \mathbf{r})_\alpha (\mathbf{r}' - \mathbf{r})_\beta / R^2. \quad (\text{A28})$$

Therefore, in cylindrical symmetry, from Eqs. (A27) and (A7) one has

$$\frac{\delta \mathbf{v} \cdot \mathbf{v}(\mathbf{r}')}{\delta \rho(\mathbf{r})} = 2v(\varrho') \omega_n(|\mathbf{r}' - \mathbf{r}|) \hat{\varrho}'(\mathbf{r}' - \mathbf{r})/R \quad (\text{A29})$$

$$= \frac{v(\varrho')}{\varrho' R} \omega_n(|\mathbf{r}' - \mathbf{r}|) (\varrho'^2 - \varrho^2 + (\mathbf{r}' - \mathbf{r})^2 - (z' - z)^2), \quad (\text{A30})$$

while in spherical symmetry we obtain

$$\frac{\delta \mathbf{v} \cdot \mathbf{v}(\mathbf{r}')}{\delta \rho(\mathbf{r})} = \frac{v(r')}{r' R} \omega_n(|\mathbf{r}' - \mathbf{r}|) (r'^2 - r^2 + (\mathbf{r}' - \mathbf{r})^2). \quad (\text{A31})$$

Expressions involving tensor weighted densities become more complex but can be conveniently evaluated by taking advantage of the symmetry of the problem. For instance, in cylindrical symmetry, from Eqs. (A28) and (A14) one has

$$\begin{aligned} \frac{\delta \text{Tr}[\mathbf{T}^2](\mathbf{r}')}{\delta \rho(\mathbf{r})} &= \frac{1}{2R^2} \omega_n(|\mathbf{r}' - \mathbf{r}|) (4A(\varrho') ((\mathbf{r}' - \mathbf{r})^2 \\ &\quad - (z' - z)^2) + B(\varrho') (\varrho'^2 - \varrho^2 + (\mathbf{r}' - \mathbf{r})^2 \\ &\quad - (z' - z)^2)^2 + 4C(\varrho') (z' - z)^2). \end{aligned} \quad (\text{A32})$$

3. Calculation of $c^{(1)}(\mathbf{r})$

The one-body direct correlation function $c^{(1)}(\mathbf{r})$ is obtained from Eq. (18) and the results of the preceding subsections. The steps required to obtain $c^{(1)}(\mathbf{r})$ are completely similar to the ones made for obtaining the m_i 's, and therefore all calculations can be conveniently carried out in Fourier space by means of the convolution theorem.

APPENDIX B: DISCRETE FOURIER AND HANKEL TRANSFORMS

The Fourier transform is defined by

$$\tilde{f}(\mathbf{k}) = \int f(\mathbf{r}) \exp(i\mathbf{k} \cdot \mathbf{r}) d\mathbf{r}, \quad (\text{B1})$$

while

$$f(\mathbf{r}) = \frac{1}{(2\pi)^{\mathcal{D}}} \int \tilde{f}(\mathbf{k}) \exp(-i\mathbf{k} \cdot \mathbf{r}) d\mathbf{r} \quad (\text{B2})$$

represents the inverse Fourier transform (\mathcal{D} is the dimension). In three dimensions, when the function to be transformed has radial symmetry, i.e., $f(\mathbf{r})=f(r)$, the Fourier transform can be rewritten as

$$F(k) = \frac{4\pi}{k} \int_0^\infty r f(r) \sin(kr) dr, \quad (\text{B3})$$

and its inverse Fourier transform is then given by

$$f(r) = \frac{1}{2\pi^2 r} \int_0^\infty k F(k) \sin(kr) dk. \quad (\text{B4})$$

Therefore, in this case, $rf(r)$ and $kF(k)$ are related through sine transforms. These transforms can be easily computed moving to discrete space and using a fast Fourier transform procedure.

For radial symmetry in two dimensions ($f(\mathbf{r})=f(\varrho)$), the Fourier transform is given by

$$F(q) = 2\pi \int_0^\infty \varrho f(\varrho) J_0(q\varrho) d\varrho, \quad (\text{B5})$$

with J_0 being the zeroth order Bessel function of the first kind, while the inverse Fourier transform is given by

$$f(\varrho) = \frac{1}{2\pi} \int_0^\infty q F(q) J_0(q\varrho) dq. \quad (\text{B6})$$

Transforms (B5) and (B6) are examples of Hankel transforms, also known as Fourier-Bessel transforms. In order to evaluate the transforms, we consider the procedure described by Ref. 44 which is here briefly outlined. Let us assume that $f(\varrho)$ can be written as a series

$$f(\varrho) \approx \sum_{i=1}^m F_i J_0(q_i \varrho), \quad (\text{B7})$$

with m being the number of zeros of J_0 to be employed, F_i some given coefficients, and $q_i = z_i / \varrho_M$, with z_i the i th zero of J_0 and ϱ_M the cutoff distance in real space. Inserting (B7) in (B5), we get

$$F(q_j) \approx 2\pi \sum_{i=1}^m F_i \int_0^{\varrho_M} J_0(q_j \varrho) J_0(q_i \varrho) \varrho d\varrho. \quad (\text{B8})$$

In order to solve this integral, one has to remember the orthogonality relationship

$$\int_0^1 J_0(z_i x) J_0(z_j x) x dx = \frac{1}{2} J_1^2(z_i) \delta_{ij}, \quad (\text{B9})$$

where J_1 represents the first order Bessel function of the first kind and δ_{ij} is the usual Kronecker's delta function. Applying (B9) and (B8), one obtains

$$F(q_j) = \pi \varrho_M^2 J_1^2(z_j) F_j, \quad (\text{B10})$$

which allows us to know the coefficients F_j in (B7) and rewrite it as

$$f(\varrho_i) = \sum_{j=1}^m \frac{J_0(q_j \varrho_i)}{\pi \varrho_M^2 J_1^2(z_j)} F(q_j). \quad (\text{B11})$$

Equation (B11) represents the inverse discrete Hankel transform. If we repeat the calculations assuming

$$F(q) \approx \sum_{i=1}^m f_i J_0(q \varrho_i), \quad (\text{B12})$$

with $\varrho_i = z_i / q_M = z_i \varrho_M / z_m$, we arrive at the direct discrete Hankel transform,

$$F(q_j) = \sum_{i=1}^m \frac{4\pi J_0(q_j \varrho_i)}{q_M^2 J_1^2(z_i)} f(\varrho_i). \quad (\text{B13})$$

Transforms (B13) and (B11) can be easily implemented in the computer program. The transform kernel including $J_0(q_j \varrho_i) / J_1^2(z_i)$ is computed once at the start of the program and then reused every time a Hankel transform is needed.

- ¹Y. Rosenfeld, Phys. Rev. Lett. **63**, 980 (1989).
- ²Y. Rosenfeld, Phys. Rev. A **42**, 5978 (1990).
- ³Y. Rosenfeld, J. Chem. Phys. **98**, 8126 (1993).
- ⁴E. Kierlik and M. L. Rosinberg, Phys. Rev. A **42**, 3382 (1990).
- ⁵E. Kierlik and M. L. Rosinberg, Phys. Rev. A **44**, 5025 (1991).
- ⁶E. Kierlik, M. L. Rosinberg, J. E. Finn, and P. A. Monson, Mol. Phys. **75**, 1435 (1992).
- ⁷S. Phan, E. Kierlik, M. L. Rosinberg, B. Bildstein, and G. Kahl, Phys. Rev. E **48**, 618 (1993).
- ⁸Y. Rosenfeld, M. Schmidt, H. Löwen, and P. Tarazona, J. Phys.: Condens. Matter **8**, L577 (1996).
- ⁹Y. Rosenfeld, M. Schmidt, H. Löwen, and P. Tarazona, Phys. Rev. E **55**, 4245 (1997).
- ¹⁰P. Tarazona and Y. Rosenfeld, Phys. Rev. E **55**, R4873 (1997).
- ¹¹J. A. Cuesta, Phys. Rev. Lett. **76**, 3742 (1996).
- ¹²J. A. Cuesta and Y. Martínez-Ratón, Phys. Rev. Lett. **78**, 3681 (1997).
- ¹³J. A. Cuesta and Y. Martínez-Ratón, J. Chem. Phys. **107**, 6379 (1997).
- ¹⁴A. González, J. A. White, and R. Evans, J. Phys.: Condens. Matter **9**, 2375 (1997).
- ¹⁵A. González and J. A. White, Physica A **296**, 347 (2001).
- ¹⁶M. Schmidt, J. Phys.: Condens. Matter **11**, 10163 (1999).
- ¹⁷M. Schmidt, H. Löwen, J. M. Brader, and R. Evans, Phys. Rev. Lett. **85**, 1934 (2000).
- ¹⁸M. Schmidt, Phys. Rev. E **60**, R6291 (1999).
- ¹⁹M. Schmidt, Phys. Rev. E **62**, 3799 (2000).
- ²⁰M. Schmidt, Phys. Rev. E **62**, 4976 (2000).
- ²¹P. Tarazona, Phys. Rev. Lett. **84**, 694 (2000).
- ²²P. Tarazona, Physica A **306**, 243 (2002).
- ²³J. A. Cuesta, Y. Martínez-Ratón, and P. Tarazona, J. Phys.: Condens. Matter **14**, 11965 (2002).
- ²⁴L. Lafuente and J. A. Cuesta, J. Phys.: Condens. Matter **14**, 12079 (2002).
- ²⁵R. Roth, R. Evans, A. Lang, and G. Kahl, J. Phys.: Condens. Matter **14**, 12063 (2002).
- ²⁶Y. X. Yu and J. Z. Wu, J. Chem. Phys. **117**, 10156 (2002).
- ²⁷R. Roth and S. Dietrich, Phys. Rev. E **62**, 6926 (2000).
- ²⁸T. Boublík, J. Chem. Phys. **53**, 471 (1970).
- ²⁹G. A. Mansoori, N. F. Carnahan, K. E. Starling, and T. W. Leland, Jr., J. Chem. Phys. **54**, 1523 (1971).
- ³⁰A. González, J. A. White, F. L. Román, S. Velasco, and R. Evans, Phys. Rev. Lett. **79**, 2466 (1997).
- ³¹A. González, J. A. White, F. L. Román, and R. Evans, J. Chem. Phys. **109**, 3637 (1998).
- ³²J. A. White, A. González, F. L. Román, and S. Velasco, Phys. Rev. Lett. **84**, 1220 (2000).
- ³³A. González, J. A. White, F. L. Román, and S. Velasco, J. Chem. Phys. **120**, 10634 (2004).
- ³⁴A. González, F. L. Román, and J. A. White, J. Phys.: Condens. Matter **11**, 3789 (1999).
- ³⁵P. Bryk, R. Roth, M. Schoen, and S. Dietrich, Europhys. Lett. **63**, 233 (2003).
- ³⁶P. Bryk, R. Roth, K. R. Mecke, and S. Dietrich, Phys. Rev. E **68**, 31602 (2003).
- ³⁷P. M. König, P. Bryk, K. Mecke, and R. Roth, Europhys. Lett. **69**, 832 (2005).
- ³⁸S. Figueroa-Gerstenmaier, F. J. Blas, J. B. Avalos, and L. F. Vega, J. Chem. Phys. **118**, 830 (2003).
- ³⁹Y. X. Yu and J. Z. Wu, J. Chem. Phys. **119**, 2288 (2003).
- ⁴⁰N. F. Carnahan and K. E. Starling, J. Chem. Phys. **51**, 635 (1969).
- ⁴¹R. Evans, in *Inhomogeneous Fluids*, edited by D. Henderson (Dekker, New York, 1992), p. 85.
- ⁴²D. Frenkel and B. Smit, *Understanding Molecular Simulation: From Algorithms to Applications* (Academic, London, 1996).
- ⁴³F. L. Román, J. A. White, A. González, and S. Velasco, J. Chem. Phys. **124**, 154708 (2006).
- ⁴⁴F. Lado, J. Chem. Phys. **49**, 3092 (1968).